

# Hybrid 3D printing of bio-inspired artificial slowly adapting type II afferents

Received: 25 August 2024

Accepted: 13 August 2025

Published online: 26 September 2025

 Check for updatesMina Lee , Michael Sotzing, Jue Wang  & Alex Chortos  

Neuromorphic sensory systems could provide low power consumption and direct electrical integration with biological systems. However, the complex fabrication of these multicomponent systems limits fabrication throughput and prototyping flexibility. To fabricate a slowly adapting type II artificial afferent nerve, this work introduces a hybrid direct write 3D printing approach that uses the pick and place of a surface mount ring oscillator to generate voltage pulses and an engineered quantum tunneling composite as a strain sensor. Our quantum tunneling sensor composition includes oil to increase the strain range and reduce the hysteresis compared to traditional quantum tunneling composites. The sensing composite provides a resistance change of over 6 orders of magnitude with a strain range of over 50%. Our approach enables rapid prototyping of 3D artificial sensory systems with potential applications in prosthetics and robotics.

Neuromorphic systems, which take inspiration from biological nervous systems, are sought to mimic the energy efficiency and adaptability of biology<sup>1,2</sup>. Using bio-inspired electrical signals enables edge computing, in which sensor signals are processed locally<sup>3–5</sup>, and creates the possibility of transferring information between technological and biological systems<sup>6–8</sup>. Neuromorphic concepts are contributing to functional advancements in rapidly expanding fields such as Human-Machine Interfaces, soft robotics, and biomedical devices<sup>9–11</sup>, motivating the proliferation of devices that include artificial sensory neurons<sup>12,13</sup>, neuromorphic efferent nerves<sup>11</sup>, optical neuron devices<sup>14,15</sup>, and neural interface systems<sup>16</sup>.

The afferent nerve transmits sensory information from the body to the central nervous system, allowing us to interact with the environment<sup>17</sup>. These biological sensory nerves consist of a sensory receptor, axon, and cell body (Fig. 1a), which convert stimulus magnitude into frequency-modulated action potentials (voltage pulses) with constant amplitude that provide efficient and high-fidelity signal transmission. To detect the stimulus, the receptor must reach a certain intensity threshold, after which the frequency of action potentials increases with increasing stimulus intensity. These allow the nervous system to encode and process different intensities of sensory input with high precision. After artificial afferent nerves (AANs) were recognized for their potential in research and treatment avenues for diseases, developing AANs has

sparked great enthusiasm<sup>18–21</sup>. Early flexible AANs used organic ring oscillators to generate the artificial action potentials and flexible pressure sensors to modulate the frequency<sup>8</sup>. Subsequent work included an artificial synapse to aggregate signals from multiple receptors and mimic a reflex arc in a biohybrid system<sup>13</sup>. These devices were fabricated by manually integrating different device functions onto a device. This challenge was addressed through monolithic integration of an ANN by fabricating devices in a stretchable form factor<sup>22</sup>. Since the most challenging function of an ANN is the generation of voltage pulses, several groups use traditional circuits to accomplish this function<sup>23,24</sup> with the limitation that these devices were on a separate substrate. Despite major progress, this field faces two main limitations. First, most studies have focused on emulating the Slowly Adapting type I (SA-I) mechanoreceptor, which detects static pressure<sup>25–27</sup>. Biological skin also includes the Slowly Adapting type II (SA-II) mechanoreceptor that measures skin stretch and is essential for proprioception (feedback for controlling body positioning). Secondly, the fabrication processes are often time-consuming and include manual steps that can limit reproducibility. AANs require multiple functions that include transduction and the generation of biomimetic signals, requiring several device components and multiple materials<sup>28–30</sup>. Hence, there is an urgent need to develop a simplified and automated manufacturing method, making AAN more accessible, reproducible, and cost-effective.

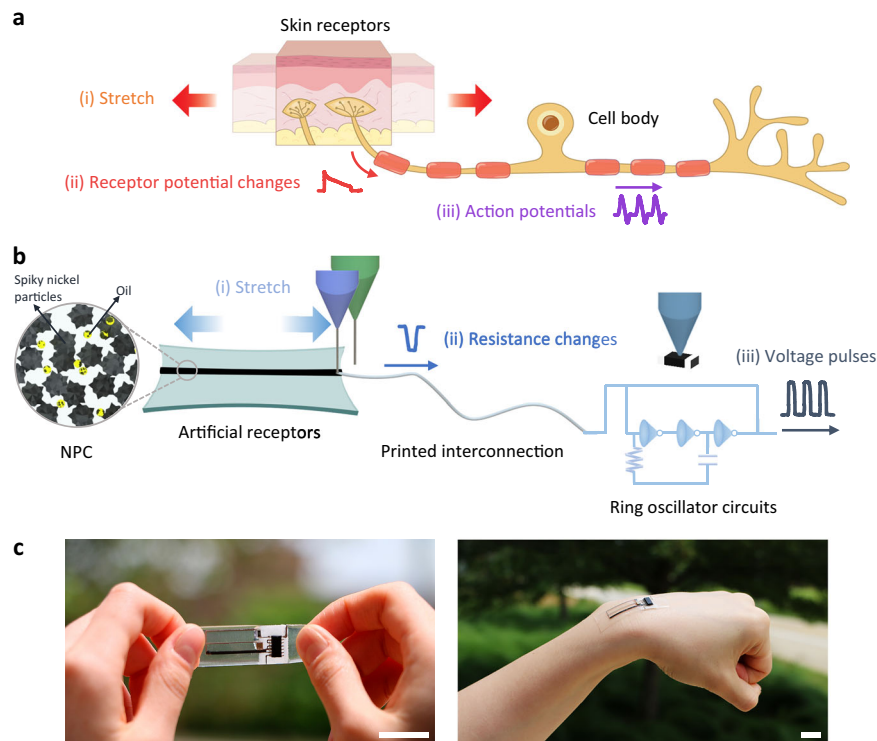


**Fig. 1 | Biological and artificial afferent nerves.** **a** Schematic of biological afferent nerve. When stretching is applied to the skin, the SA-II mechanoreceptor in the biological afferent nerve responds by changing its receptor potential. The cell body processes the changes in receptor potential, converting them into action potentials that encode stretching information, which is then relayed to the central nervous system. **b** Schematic of artificial afferent nerve. In an artificial afferent nerve, the

application of strain changes the resistance of the negative piezoresistive composite (NPC). This change is transmitted by printed conductive interconnections. The ring oscillator circuits transform this change into an electrical signal including strain information. **c** Images of the hybrid 3D printed artificial SA-II afferent nerve. Scale bars, 20 mm.

In this work, we fabricate a stretchable ANN that replicates the properties of the SA-II receptor using hybrid 3D printing (Fig. 1b). Hybrid fabrication combines the advantages of high-performance circuits made using conventional lithography manufacturing with the advantages of printed electronics for creating deformable, large area, or multimaterial/multifunctional systems<sup>30–33</sup>. Our fabricated AAN system leverages the mechanical compliance and strain sensitivity of the printed sensor composite and the signal stability of traditional silicon-based integrated circuits (Fig. 1c). Bio-mimetic electrical signals are created by a ring oscillator composed of surface-mounted device (SMD) inverters (Fig. 1b). While most previous work has modulated the output frequency of oscillators by changing the supply voltage<sup>13,22</sup>, this approach has the drawback that the frequency and amplitude of the pulses are both modulated, which is not the case for biological or digital systems. In addition, the resulting ANNs have a lower limit for the oscillation frequency, effectively truncating the signal from the low stimulus range. In contrast, our approach modulates frequency through an engineered strain sensor that changes the resistance-capacitance (RC) time constant in the oscillator feedback loop. The frequency output of the oscillator is inversely related to RC. Consequently, to achieve a biomimetic frequency signal that increases from zero to several hundred Hz with increasing strain, the resistance of the strain sensor must decrease by several orders of magnitude over the desired strain range. This contrasts with typical strain sensors, which show increased resistance with strain (positive piezoresistance). Therefore, we developed a negative piezoresistive composite (NPC) based on the quantum tunneling effect that displays the requisite decrease in resistance of ~6 orders of magnitude, enabling biomimetic signals from the ANN. Quantum tunneling composites consist of spiky conductive particles in an insulating elastomer matrix. The spikes on the particles locally concentrate the electric field, and the resulting

non-linear quantum tunneling between particles gives rise to the negative piezoresistance. Previous quantum tunneling compositions are limited by low elongation at break and high hysteresis, limiting their effectiveness in strain-sensing applications<sup>34–37</sup>. These limitations are mitigated in our NPC by including oil in the polymer phase of the composite, making it a breakthrough advancement in quantum tunneling based strain sensors. This material innovation, combined with our hybrid 3D printing platform, enables potential applications in robotic sensor feedback, prosthetics, and bio-integrated devices.

## Results

### Engineered NPC with stretch-responsive and low hysteresis properties

When the SA-II receptor detects stretching, it generates a receptor potential, the initial electrical response in a sensory cell upon encountering a stimulus (Fig. 1a)<sup>38</sup>. The receptor potential is characterized by two main features. First, it has a threshold that activates the receptor only when deformations exceed a biomechanically significant level, preventing unnecessary power consumption with minor stimuli. Beyond this threshold, the output of the receptor is proportional to the stimulus<sup>39</sup>. To mimic these biological features, our artificial SA-II receptor is made of an NPC that utilizes a quantum tunneling effect (Supplementary Fig. 1). This rapidly increases conductivity once a certain threshold strain is reached.

The engineered NPC consists of a polyurethane acrylate polymer (PUA), spiky nickel particles, and oil (Fig. 1b). We choose polyurethane acrylate as the elastomer phase for its high elongation at break<sup>40</sup>, enabling large composite strains. Spiky particles are crucial for facilitating the quantum tunneling effect. In conventional composites, the transition from an insulating state to a conductive state requires the formation of percolation networks wherein conductive fillers must

physically contact each other to facilitate electron transport via established electrical pathways. However, in composites containing fillers with surface asperities, the acuminate points significantly enhance electric field concentration at these junctures and reduce the barrier potential required for electron transmission. This promotes a quantum tunneling phenomenon, where electrons can pass through the interstitial spaces between fillers without direct physical contact<sup>34,41,42</sup>. Application of mechanical strain induces a change by the Poisson effect, specifically reducing the transverse dimensions of the composites<sup>43,44</sup>. This deformation results in a diminished inter-particle distance, facilitating more effective electron tunneling across the reduced barriers. In our composite, an essential and innovative component is the oil. We used dioctyl phthalate as an oil because of its compatibility with the PUA (Supplementary Fig. 2). Previous quantum tunneling composites have typically consisted of a polymer matrix and spiky fillers, exhibiting a low dynamic range<sup>37,42</sup> or large hysteresis<sup>34,45</sup> due to internal friction generated by the motion of polymer molecular chains and nickel particles<sup>34,46</sup>. In contrast, the addition of oil to our NPC composition can significantly increase the dynamic range to more than 50% strain and reduce hysteresis.

To illustrate the advantage of this composition, we compared our NPC composition to two controls: a traditional quantum tunneling composite composed of Ni particles in polydimethylsiloxane (PDMS)<sup>37,43–45</sup> and a composition of Ni particles in PUA with no oil (Supplementary Figs. 3, 4). The standard PDMS-based composite exhibited a low elongation at break (~40% strain) and significant drift during cycling. Specifically, cyclic measurements conducted under 20% strain for four cycles revealed a two-order magnitude decrease in conductivity for the PDMS-based composite, indicating poor repeatability. The PUA-based, while achieving a higher elongation at a break of 50% strain, still experienced substantial drift with a one-order magnitude decrease in conductivity under the same cyclic conditions. In contrast, the NPC containing oil provided a large dynamic range with improved repeatability between cycles. The conductivity of the NPC composite decreased only marginally during cyclic measurements under 20% strain. These findings are further summarized in Supplementary Table 1, which compares the key characteristics of reported NPCs. This shows that our NPC achieves a broad dynamic strain range, a large resistance change, and stable electrical performance across cycles, distinguishing it from earlier quantum tunneling composites and highlighting its suitability for mimicking biological SA-II receptors.

To elucidate the role of composition on the electromechanical properties of the NPC, we measured electrical response under mechanical strain while varying the ratios of nickel particles, oil content, and crosslinking density within the NPC (Fig. 2; and Supplementary Table 2). First, we found that the nickel particle ratio significantly influenced the overall conductivity, especially OFF/ON conductivity (Fig. 2a, d, g). The OFF conductivity the value at low strain. The ON conductivity is the value at 50% strain. We maintained a consistent amount of polymer and oil, while varying the content of spiky nickel fillers within the composite from 60 wt% to 71.4 wt%. With 60 wt% nickel particles, the OFF conductivity was measured as  $2.79 \times 10^{-5} \text{ S m}^{-1}$  and the ON conductivity reached  $5.95 \text{ S m}^{-1}$ . When we increased the nickel content to 71.4 wt%, the OFF conductivity rose to  $0.064 \text{ S m}^{-1}$  and the ON conductivity increased to  $117.58 \text{ S m}^{-1}$ . An overall change in conductivity magnitude increased with increasing nickel particles, suggesting that the overall conductivity of the composite is predominantly governed by the concentration of fillers.

To explore the dependency on oil content, we kept the amounts of nickel fillers constant while varying the weight ratio between polymer and oil from 1:0 to 1:3 (Fig. 2b, e, h). Without oil, the conductivity change spanned 3.67 orders of magnitude, but this expanded to 5.99 orders when the oil content was increased to 25 wt%. The increased oil ratio increased the range of conductivity change. We hypothesize that

the oil acts as a lubricant among the nickel particles, significantly reducing friction between them. This reduction in friction enhances the mobility of the nickel particles, allowing them to move more freely within the composite. Such enhanced mobility is crucial because it facilitates the repositioning of fillers more effectively when the composite undergoes deformation. This increased particle mobility also leads to a greater ability of the nickel particles to adapt their positions and form conductive pathways under different mechanical stresses, thereby broadening the range of conductivity change observed in the composite<sup>47,48</sup>.

Furthermore, we investigated the effect of crosslink density on the electromechanical properties (Fig. 2c, f, i) using dithiols to modulate the crosslinking. While acrylate groups usually polymerize to form chains that act as crosslink sites that link multiple polymer chains, dithiols link only two acrylate groups, extending the two chains to create a longer chain<sup>49</sup>. Therefore, we increase the amount of dithiol to achieve a lower crosslinking density. We varied the dithiol from 0 wt% to 0.3 wt% and compared the strain required to reach a conductivity of  $10^{-3} \text{ S m}^{-1}$ . The strain value increased from 3.49% strain without dithiol to 13.31% strain with 0.3 wt% of dithiol. This increase in strain with a decrease in crosslinking density demonstrates that the material decreases sensitivity to small deformations and withstands more strain before its internal structure and conductivity are significantly affected<sup>50</sup>.

The introduction of dithiols could raise concerns about long-term stability due to the transient nature of some sulfur bonds<sup>51</sup>, so we assessed the time-dependent behavior of the composite (Supplementary Fig. 5). Samples containing 0.2 wt% dithiol were tested immediately after fabrication and after 50 days of ambient storage. Both samples exhibited similar ON/OFF conductivity and strain-dependent resistance behavior with a resistance change of 6 orders of magnitude. These results confirm that the inclusion of dithiol, while effective in tuning crosslink density, does not compromise long-term stability. The composite maintains its mechanical and electrical integrity over time, reinforcing the reliability of this approach for durable, strain-responsive sensing applications.

In summary, the concentration of fillers had the largest effect on the conductivity. The oil concentration within the composite altered NPC's dynamic range of conductivity. We also showed that adjusting the cross-linking density of the polymer can change the NPC's strain sensitivity. These findings collectively highlight that the engineered NPC material has tunability, allowing for the independent tuning of its key electrical properties: ON/OFF conductivity, conductivity order change, and onset strain, through compositional variations (Supplementary Fig. 6). This enhances the material's versatility, offering a wide spectrum of design possibilities for AANs. As a result, this offers broad application potential and customization capabilities in sensory systems for artificial devices, enabling the creation of highly adaptive and responsive technologies tailored to diverse functional requirements.

### Printed artificial SA-II mechanoreceptor

Using this engineered NPC, we fabricated artificial SA-II receptors (Fig. 3a). We utilized direct ink writing (DIW) with a nozzle diameter of  $410 \mu\text{m}$ . When composite materials are extruded by DIW, the interaction with the nozzle's shear force can induce particle rearrangement<sup>52</sup>, potentially altering the electrical properties. However, our printed NPC maintained the major characteristics of the receptor potential which is a change in resistance of  $10^6$ -fold under 50% strain, confirming that the DIW fabrication is suitable. NPC materials printed parallel and perpendicular to the direction of applied strain show similar properties (Supplementary Fig. 7), further supporting the compatibility with DIW printing. Stable electrical properties were also confirmed through cyclic testing for 100 cycles under 50% strain (Fig. 3b). Although a slight initial increase in resistance was observed during the first 15 cycles, it subsequently stabilized after this conditioning period.

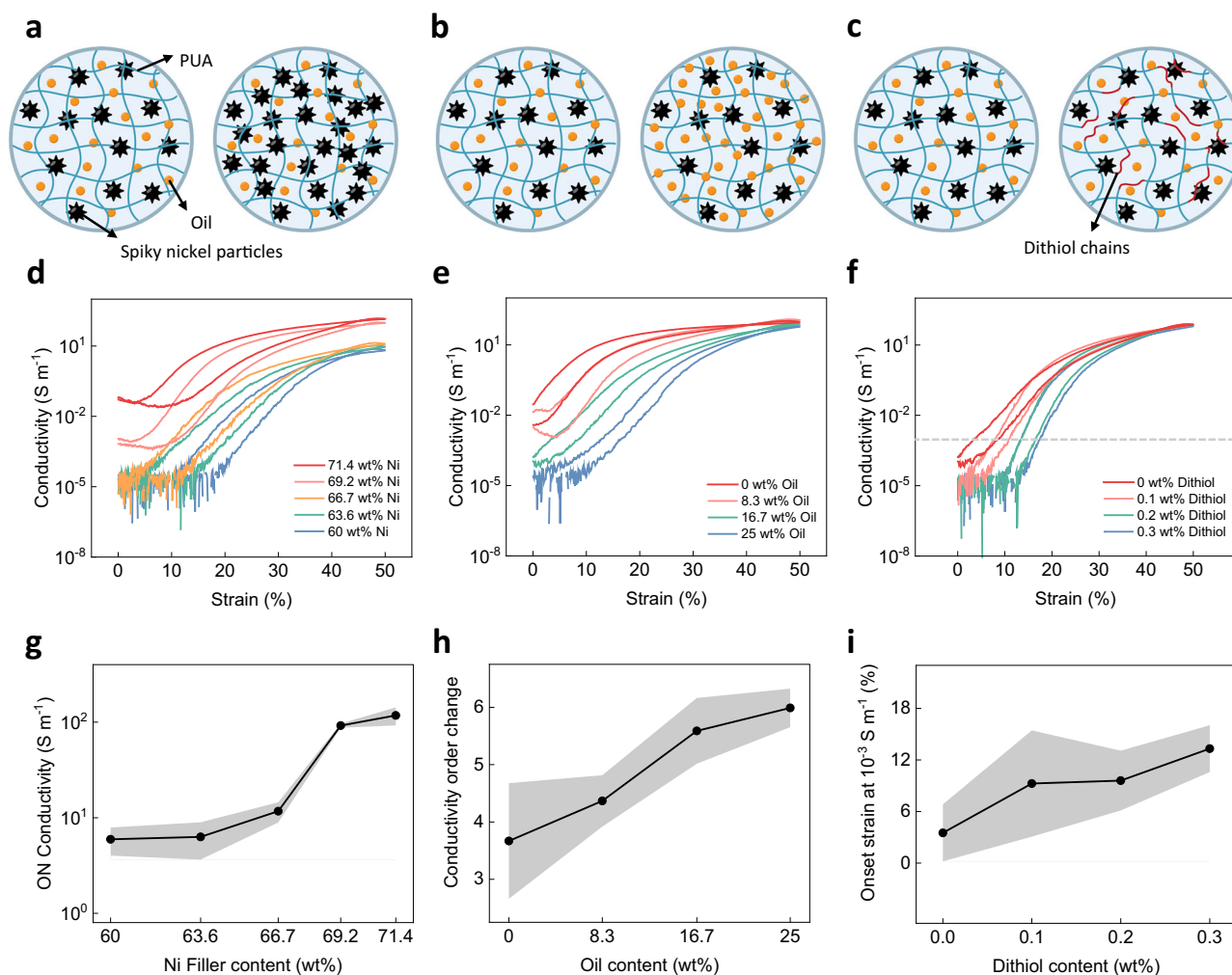


**Fig. 2 | Electromechanical characterization of the NPC.** Schematic illustration showing variations in (a) nickel particle ratios, (b) oil content ratios, and (c) dithiol content ratios. Conductivity response curved for NPC with varying (d) nickel particle ratios, (e) oil content ratios, and (f) dithiol content ratios. The dashed horizontal line indicates a conductivity of  $10^{-3} \text{ S m}^{-1}$ . g Conductivity values at 50% strain

(ON conductivity) corresponding to different nickel particle ratios. h Conductivity order change with varying oil content ratios. i Strain at which conductivity reaches  $10^{-3} \text{ S m}^{-1}$  in the forward sweep as a function of dithiol content ratios. In (g–i), the black dots represent the average of three samples and the gray represents the standard deviation.

Receptor potentials are graded and are proportional to the strength of the stimulus that evokes them<sup>53</sup>, a crucial feature for accurately sensing and conveying stimulus intensity. To verify this in the artificial SA-II receptor, cyclic measurements were taken at incremental strains from 10% to 50%, with each strain level tested across three cycles (Fig. 3d; and Supplementary Fig. 8). At 10% strain, the resistance change was not recorded and remained stable. This resistance change escalated to 2.73 orders at 20% strain and the most notable increase was observed at 50% strain, where the resistance change jumped to 4.95 orders. Further validation was conducted through a ramp response test (Supplementary Fig. 9), in which the sensor demonstrated rapid activation within one second and produced distinct on-conductivity magnitudes corresponding to each applied strain level. Notably, the sensor maintained consistent responses across various strain rates ranging from  $60\% \text{ s}^{-1}$  to  $160\% \text{ s}^{-1}$  (Supplementary Fig. 10). This rate-independent behavior suggests that the inclusion of oil in the composite effectively provides low viscoelasticity, which often compromises sensing reliability under dynamic conditions. These results confirm that the artificial SA-II receptor exhibits biologically relevant sensing behavior and maintains robustness under varying mechanical input, making it a strong candidate for practical applications in bioinspired tactile sensing.

Biological SA-II receptors are selectively sensitive to strain. We measured the sensitivity of the artificial receptor to other stimuli including pressure, bending, and twisting. We first conducted a series of tests, comparing its response to finger pressing, twisting, bending, and stretching (Fig. 3c). This demonstrated that the receptor's resistance changes were considerably more pronounced when subjected to stretching, compared to the minimal changes observed with other stimuli. To further refine our understanding, we also conducted experiments focusing on the pressure and bending to which the system would be more frequently exposed during use. In the pressure tests, we applied forces ranging from 0 Pa to 25 kPa. It did not show significant resistance changes, indicating the receptor's relative insensitivity to pressure (Fig. 3e). Similarly, for the bending tests, we employed a linear actuator to induce deformations ranging from 0 to 200 degrees. This also failed to produce notable resistance variations (Fig. 3f).

#### Circuit design and ink preparation for SA-II AAN system

To make the SA-II AAN system, it is essential to include components that can convert receptor potential into action potentials. The frequency of action potentials serves as the primary feature for efficient transmission of stimulus information<sup>13</sup>. To emulate this, we designed a



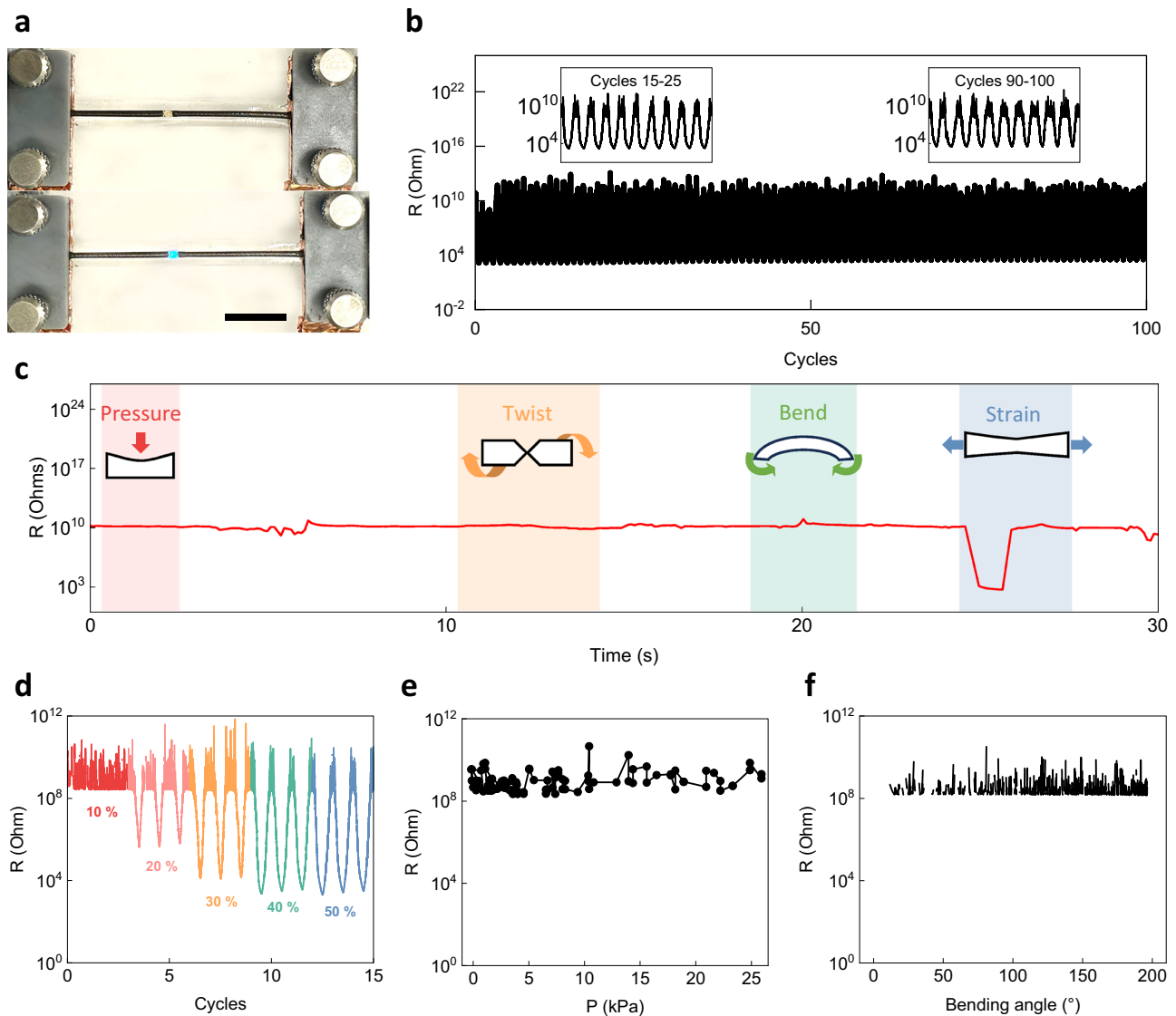


**Fig. 3 | Sensing characteristics of the artificial mechanoreceptor.** **a** Image illustrating how the artificial mechanoreceptor triggers an LED switch; as the receptor stretches and its resistance decreases, the LED turns on (scale bar: 10 mm). **b** Cyclic stability test of artificial mechanoreceptor under 50% strain for 100 cycles. The insets highlight cycles 15 to 25 and the final 10 cycles. **c** Responsive curve of the

artificial mechanoreceptor to different stimuli; finger pressure, twist, bend, and tensile strain. **d** Resistance changes under cyclic strains at different strain ranges. **e** Resistance changes in response to different pressure levels. **f** Resistance changes at varying bending angles.

circuit that consists of a ring oscillator and resistor-capacitor (RC) feedback circuit (Fig. 4a). The resistance change generated by the artificial SA-II mechanoreceptor alters the charging time of the capacitor in the RC circuit, which in turn affects the output voltage's oscillation frequency ( $f$ ) according to Eq. (1).

$$f = \frac{1}{2R_1C_1 \left( \frac{0.405R_2}{R_1 + R_2} + 0.693 \right)} \quad (1)$$

where  $R_1$  and  $C_1$  are resistance and capacitance in RC feedback and  $R_2$  is resistance from the artificial afferent receptor.

The resistance and capacitance values in the RC circuit were chosen based on Eq. (1) to tune the frequency to match the range of biological afferent nerves (0 to around 100 Hz)<sup>54</sup>. Using the resistance change from the NPCs ranging from  $10^7$ – $10^2 \Omega$ , a resistance of  $R_1 = 1 \text{ k}\Omega$  and a capacitance of  $C_1 = 10 \mu\text{F}$  were identified as optimal for the circuit's design. The measured frequency variation was in good agreement with the analytical result. The circuit produced a square voltage

waveform (Fig. 4b), with a frequency modulation ranging from 0 Hz to 106.87 Hz, consistent with the analytical expectations ranging from 0.07 Hz to 140.18 Hz (Fig. 4c). The stable frequency output across a wide range of frequencies emphasizes the benefits of using a hybrid approach in which high performance silicon circuits are used to generate the voltage pulses.

We also developed a set of specialized compatible inks to enable hybrid printing of the ANN. These include mechanical substrate inks and conductive ink essential for creating interconnections. A critical aspect of this fabrication process is understanding the interactions between different materials, particularly how the NPC interacts with adjacent inks. When the NPC is used in proximity to other materials, there's a risk that oils from the NPC could diffuse into the neighboring inks, which would change the sensing characteristics of the NPC. To mitigate this, we used a commercial fluorinated PDMS as the base for all other inks. Fluorinated polymers are known for their high resistance to oils, chemicals, and solvents due to the strong carbon-fluorine bonds and the low polarizability of fluorine atoms<sup>55</sup>. Therefore, the

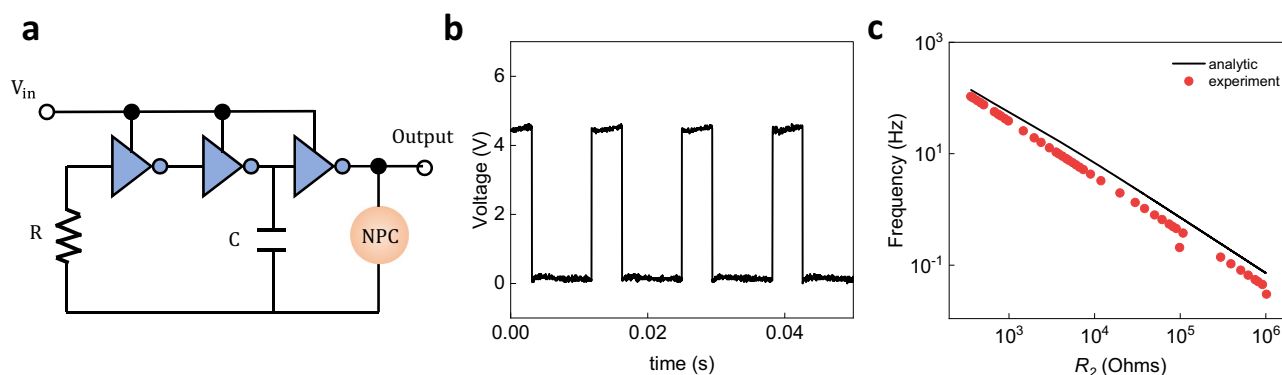


**Fig. 4 | Circuit design of SA-II AAN system.** **a** Schematic image of AAN circuit. It consists of ring oscillator, one resistor ( $R$ ), one capacitor ( $C$ ), and NPC. **b** Output voltage curve from the designed circuit. **c** Comparison of analytic model and experiment results with artificial mechanoreceptor.

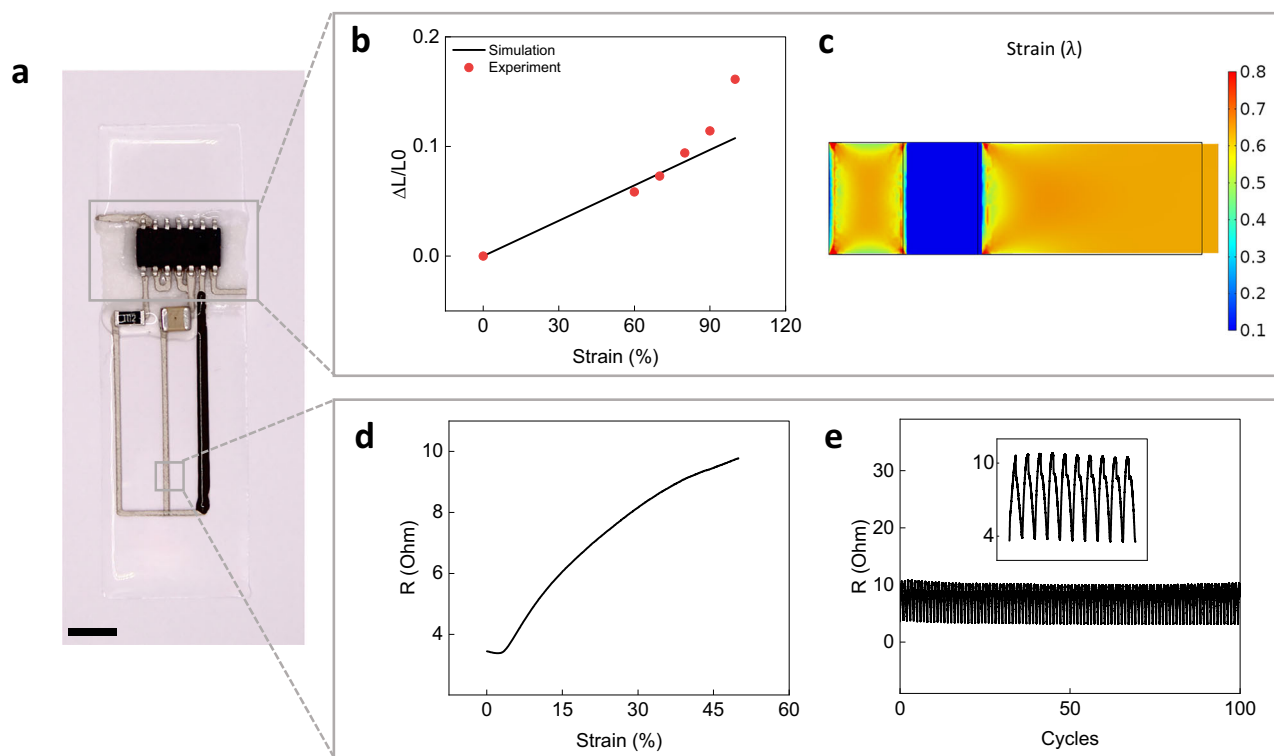


**Fig. 5 | Inks for SA-II AAN system.** **a** Image of artificial afferent nerve system (scale bar: 5 mm). **b** Mechanical characterization of the substrate used in the artificial system. Comparison of experiment results and (c) COMSOL simulation results. **d** Electromechanical characterization of conductive composite used for

interconnections between the printed artificial mechanoreceptor and surface mount electrical components. **e** Cyclic stability test of conductive composite under 50% strain for 100 cycles. The inset shows the first 10 cycles.

fluorinated polymer prevents oil molecules from migrating out of the NPC. This choice ensures the temporal stability of the system by maintaining the electrical and mechanical properties of the materials involved, preventing adverse interactions between the NPC and adjacent materials.

Our ANN design includes surface mount devices (SMDs) that are connected to stretchable conductors and the NPC. The interface between hard SMDs and soft electronics is often a limiting factor for the mechanical integrity of the system<sup>31</sup>. Consequently, we employed a strategy of substrate strain engineering to reduce the local strain surrounding the SMD components<sup>56–58</sup> (Fig. 5a). This required a soft ink and a stiffer ink. The soft substrate was made entirely of a fluorinated polymer, characterized by an elastic modulus of 0.26 MPa, and can withstand up to 150% strain. The NPC was located on this soft section, enabling it to respond to the applied substrate strain. On the other

hand, the ring oscillator SMD was placed on the stiff substrate material with an elastic modulus of 3 MPa (Supplementary Fig. 11). Due to the large difference in modulus between the soft and stiff substrate regions, the strain in the stiff regions is much lower than the global strain applied to the substrate. This design was validated through COMSOL simulations. The simulations showed that the average strain in the stiff areas of the heterogeneous material is only 5.38% under 50% strain (Fig. 5c). Experiment results also aligned with this finding (Fig. 5b). This indicates that the heterogeneous substrate design effectively limits stretching in the stiffer regions where the SMD components are mounted and allows the soft areas to remain responsive.

The connectivity between the artificial mechanoreceptor and the SMDs was facilitated by a specially engineered conductive ink. This conductive composite is designed to maintain its conductivity beyond

50% strain. To achieve this, silver flakes and multi-walled carbon nanotubes (MWCNTs) were used in a synergistic combination. Silver flakes and MWCNTs are known for their excellent contact capability under stretching due to high aspect ratios, which is crucial for maintaining conductivity under strain<sup>59</sup>. Furthermore, we increased the conductivity of the silver flakes through surface iodization, a process that increases the material's electrical conductivity by introducing iodine atoms that facilitate electron transport<sup>60</sup>. To ensure uniform dispersion of the silver flakes within the composite, a non-ionic surfactant was used. This is vital as it prevents the agglomeration of silver flakes, ensuring consistent conductivity throughout the composite. As a result, a conductive composite not only maintained a low resistance ranging from 3.44–9.77  $\Omega$  under up to 50% strain (Fig. 5d) but also exhibited stable electrical properties over extensive testing cycles, demonstrated through 100 cycles of testing under 50% strain (Fig. 5e). This level of reliability and performance is crucial for the seamless operation of the artificial mechanoreceptor system, ensuring that the electrical signals are consistently transmitted even under mechanical stress.

We further explored the rheological properties of four inks to assess their suitability for extrusion printing (Supplementary Fig. 12). Both the conductive ink and stiff substrate ink demonstrated shear-thinning behavior as their viscosities decreased with increasing shear rates. Amplitude sweep tests showed that these inks have higher storage moduli than loss moduli in the plateau region and significant yield stresses (729.6 Pa for conductive ink and 496.5 Pa for stiff substrate ink). These properties confirmed their suitability for extrusion printing. The soft substrate ink and sensor ink displayed a slight decrease in viscosity with increasing strain rate. Their amplitude sweep results indicated higher loss moduli than storage moduli, indicating that they spread during printing. This is suitable for a substrate ink that creates a continuous substrate and is acceptable for printing 2.5D circuit components.

### Hybrid 3D printed artificial SA-II afferent nerve system

Using these four compatible inks, a hybrid 3D printing methodology was employed to fabricate AANs (Supplementary Movie 1). The hybrid 3D printer integrates multi-material DIW and a pick-and-place function within a singular platform<sup>31</sup>. This has improved the efficiency of soft electronics fabrication, allowing for the concurrent deposition of multiple materials and the precise placement of surface-mounted elements. The fabrication process began with the generation of a heterogeneous substrate (Fig. 6a). The substrate underwent a curing phase to ensure its stability for subsequent layers. After curing the substrate, the artificial SA-II receptor and its interconnections with conductive ink were printed, establishing the essential network pathways for signal transmission within the AAN (Fig. 6b). The next step was the precise placement of SMDs onto the substrate, utilizing the hybrid printer's pick-and-place capability (Fig. 6c). To enhance the durability and stability of the SMDs, an additional step was introduced where a layer of fluorinated PDMS is deposited around these components. This layer acts to improve the adhesion of the SMDs to the substrate, ensuring their secure attachment and operational integrity over time.

The final printed AAN was stretchable to 50% strain, providing durability to strain, bending, and twisting (Fig. 6d–g). Just above a strain threshold of ~10%, a 5 V square electrical signal was generated, characterized by a frequency of 0.119 Hz. Notably, this signal's amplitude maintained a value of 5 V even as the strain was increased to 50% (Fig. 6h). The frequency of this output signal progressively increased with higher strains (Fig. 6i and Supplementary Fig. 13), mimicking the trends in biological action potentials. Crucially, the correlation between the applied mechanical strain and the resulting frequency changes was closely aligned with the anticipated alterations in the artificial receptor potential (Fig. 6i). This confirms the AAN's

effectiveness in replicating the sensory processes found in biology. Stable operation of the AAN with cycling (Supplementary Fig. 14) indicates the robustness of the interfaces between materials and components. Although the power consumption of the receptor is high (Supplementary Fig. 15), the power can be reduced by choosing a surface mount inverter chip with characteristics optimized for low power.

Given the electromechanical performance of the fabricated AAN system, we further evaluated its applicability in integrated soft robotic platforms where large-strain deformation sensing is essential. To demonstrate this capability, the AAN was integrated with a pneumatic soft actuator and used to monitor strain during actuation (Fig. 6j). Pneumatic actuators are commonly employed in diverse soft robotic applications such as cell stretching in mechanobiology studies and soft grippers for delicate object manipulation. The entire system, including the actuator body and the AAN system, was constructed using a single hybrid 3D printing platform (Supplementary Fig. 16 and Supplementary Movie 2). First, the pneumatic actuator was printed using a multi-material printing with three different inks: a stiff substrate ink, a soft substrate ink, and a polyethylene glycol (PEG)-based sacrificial ink. The stiff substrate ink was applied to the bottom of the actuator to enable preferential inflation under pressure. The soft substrate ink was used to construct the main soft and inflatable structure, while the PEG-based ink defined the internal cavity. All printing was performed on a hot plate to accelerate curing and preserve dimensional stability in the resulting 3D structure. And the AAN system was directly printed onto the actuator surface. Finally, the system's electronics were completed using the printer's pick-and-place function to position SMD components, which were then cured through thermal post-processing. This co-fabrication approach enhances mechanical compatibility between components, reduces assembly complexity, and enables scalable production of multifunctional soft electronic systems. Overall, the successful integration of the AAN with a functional soft actuator illustrates its potential not only as a bioinspired mechanosensory system but also as a versatile platform for next-generation soft robotics and wearable technologies.

Functionally, the printed AAN system exhibited stable and strain-dependent electrical signals during inflation and deflation cycles (Supplementary Movie 3). As the actuator inflated, the resistance of the artificial receptor decreased by up to 493 k $\Omega$  (Supplementary Fig. 17), while the output signal frequency increased from 0 Hz to 8.68 Hz (Fig. 6k). And it returned to 0 Hz upon deflation. Notably, the amplitude of the generated signal remained constant at 5 V throughout all cycles, indicating a robust and repeatable frequency-based encoding of strain. This demonstration showed the AAN system's capability as a bioinspired, frequency-encoding mechanosensory suitable for integration into real-world soft robotic systems.

While our concept was demonstrated using relatively large printing features (400  $\mu$ m nozzle), the concept could be scalable to smaller sizes by using smaller nozzles<sup>61</sup> and using pick and place of bare die chips rather than packaged surface mount chips. 3D printing provides a versatile method to prototype 3D structures using multiple materials. Follow-up work could leverage this capability to create devices that mimic the 3D structure of the skin with multiple mechanical and sensing functionalities. As opposed to traditional lithography patterning in which layers must possess compatible processing conditions, 3D printing enables direct deposition of multiple materials, providing a platform to integrate multiple sensing materials (temperature, vibration, etc.).

### Discussion

We have demonstrated an artificial SA-II mechanoreceptor fabricated using hybrid 3D printing. We designed a set of compatible inks for soft substrates, stiff substrates, and conductive materials. Using hybrid 3D printing, we created an artificial afferent nerve (AAN) system that

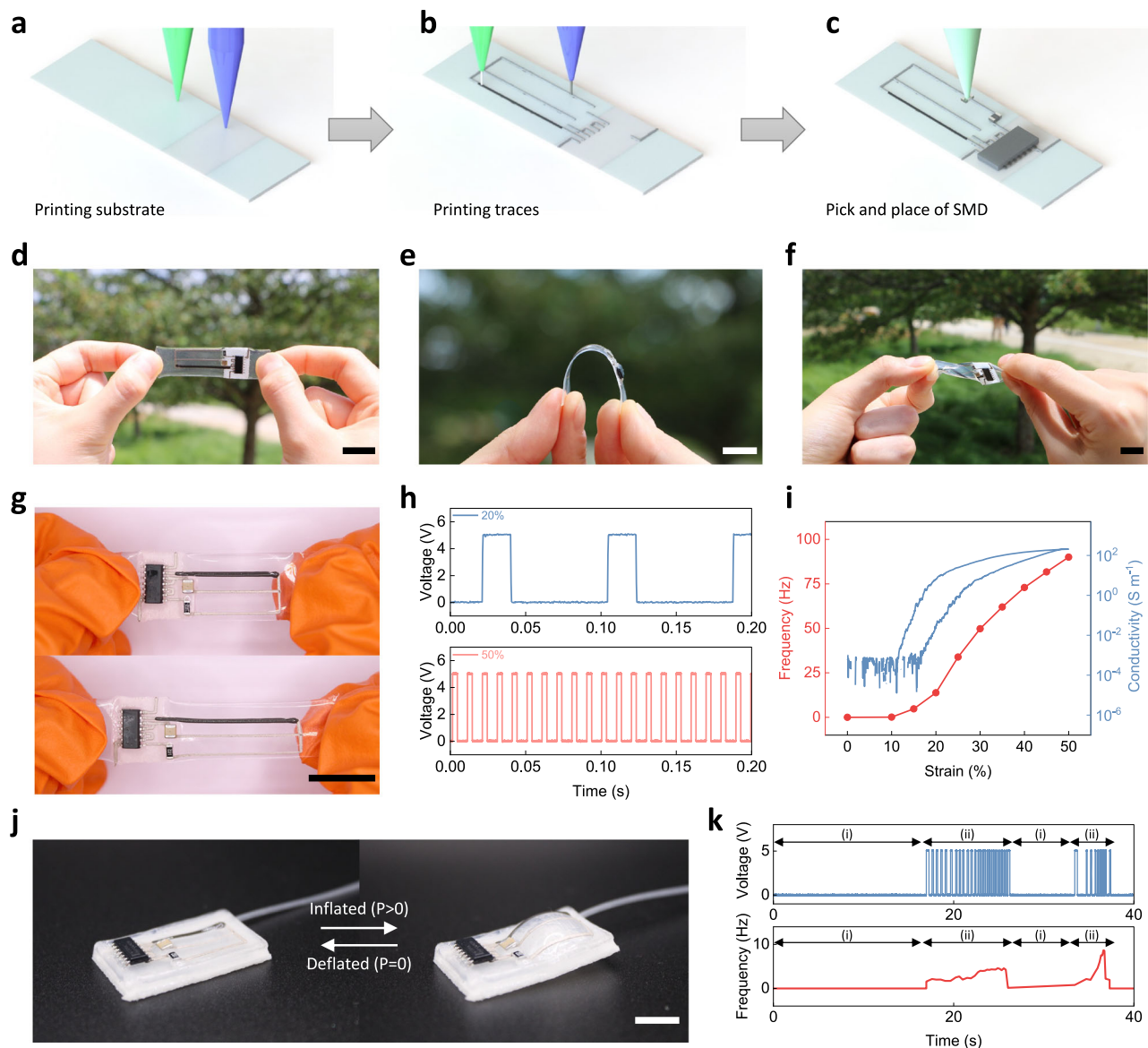


**Fig. 6 | Hybrid 3D printing and printed SA-II AAN.** Schematic images of hybrid 3D printing procedures: (a) multi-material printing of heterogeneous substrate, (b) traces including conductive interconnection and the NPC, and (c) pick and place of surface mount electrical elements. Digital images of a hybrid printed SA-II AAN system that is (d) stretchable, (e) bendable, and (f) twistable. g Images comparing a stretched and unstretched hybrid SA-II AAN system. h Output voltage curves from

printed AAN at 20% and 50% strain. i Frequency variation of output voltage from AAN system and conductivity variation from artificial mechanoreceptor.

j Operational photographs of soft pneumatic actuator with an integrated SA-II AAN system when the pressure  $P=0$  and  $P>0$ . k Output voltage curve and frequency variation of the output voltage during soft pneumatic actuator deflation (i) and inflation (ii). Scale bars, 15 mm.

incorporates a ring oscillator with an RC feedback circuit. The resistor in the RC feedback consists of a custom negative piezoresistive composite (NPC) that includes oil, allowing it to withstand up to 50% strain, exhibit low hysteresis, and provide the requisite decrease in resistance of several orders of magnitude. When the printed AAN was stretched, the frequency increased from 0 to ~100 Hz, mimicking the output of biological SA-II afferent nerves. Our artificial system represents a significant stride toward replicating the sensory functions of biological systems, with potential applications in prosthetics and robotics.

A major strength of our hybrid 3D printing is adaptability. While our current design is optimized for stretch sensing, additive fabrication allows modular integration of additional functional sensors for stimuli such as pressure, temperature, or humidity. The ability to produce 3D structures can also be leveraged to enable pressure sensitivity by changing the 3D structure of the printed components<sup>62</sup>. Incorporating a pressure-sensitive composite or tuning the sensor

geometry could allow the system to detect static pressure while maintaining stretch sensitivity. This flexibility supports future advancements in multimodal sensing, further enhancing its potential applications. Furthermore, the adaptability of the process supports enhanced scalability and accessibility. In future iterations, fabrication rate may be further enhanced by adopting in situ curing methods such as UV curing<sup>63,64</sup> or reactive printing<sup>65</sup>, which can simplify the fabrication process and reduce the need additional post-processing steps.

## Methods

### Material

Urethane acrylate oligomer (CN9018) was purchased from Sartomer. Nickel powder (APS 2.2–3.0 micron, 99.9%) was purchased from Thermo Scientific Chemicals. Dioctyl phthalate (>98.0%) and MWCNT (average diameter of 10–20 nm, average length of 5–15  $\mu\text{m}$ ) were purchased from TCI America. 2,2'-azobisisobutyronitrile (AIBN), non-



ionic surfactant (Span-80), and PEG (PEG-200) were purchased from Sigma Aldrich. Fluorinated polymer (PP2-RG04) was purchased from Gelest. Fumed silica (TS-720) was purchased from Cab-o-sil. Milled glass fibers (329; 1/16 inch) were purchased from Fibre Glast Development Corporation. Silver flake (47MR-10F) was purchased from Inframat Advanced Materials.

### Preparation of artificial mechanoreceptor ink

The negative piezoresistive ink was prepared by mixing 1 g of CN9018 with 1 g of dioctyl phthalate and 4 g of Nickel particles in a SpeedMixer (1800 rpm, 2 min). 0.0125 wt% of AIBN, a thermal initiator, was then added to the mixture. This was done by utilizing a stock solution where AIBN was already dissolved in chloroform at a concentration of 12.5 wt %. The ink mixture was mixed in the SpeedMixer for 4 min. Following this initial mixing, it was further mixed for an additional 2 min with the container left uncapped. This uncapped mixing was specifically intended to allow the chloroform to evaporate effectively. For electromechanical characterization, the ink was deposited into a dog-bone-shaped mold. For fabricating the artificial SA-II receptor, it was deposited onto cured fluorinated polymer using a hybrid 3D printer system. Both were then cured for 6 h at 60 °C in argon.

### Preparation of artificial afferent nerve system inks

To enhance adhesion to other materials, a soft substrate ink was formulated by blending a fluorinated polymer base with a curing agent at a 20:1 ratio. This mixture was processed in a SpeedMixer at 1800 rpm for 2 min to ensure thorough mixing. The stiff substrate ink was prepared by mixing 2 g of fluorinated polymer base with 0.13 g of fumed silica and 1.32 g of 1/16 inch milled glass fibers in a SpeedMixer (1800 rpm, 4 min) to ensure thorough dispersion of the particles. Subsequently, 0.2 g of the polymer's curing agent was added and the mixture was blended for an additional 2 min. To make a conductive composite, first iodized silver was required. 0.03 g of iodine was diluted in 78 g of ethanol, and then 5 g of silver flake was added to the solution. The solution was left until the water was clean, filtered, and dried under a vacuum to get iodized silver flakes. Using these flakes, the conductive ink was prepared by blending 0.6 g of fluorinated polymer base and 0.1 g of curing agent with 1.1 g of iodized silver flake, 0.008 g of MWCNT, 0.06 g of Span-80, and 0.02 g of 10% platinum catalyst for 4 min at 1800 rpm. Lastly, for the integration of the AAN system with the pneumatic actuator, the PEG-based sacrificial ink was prepared by mixing PEG with fumed silica at a weight ratio of 10:1 at 1800 rpm for 10 min.

### Characterization

The electromechanical properties of samples, including artificial mechanoreceptor and printed conductive ink, were obtained by using custom-made equipment. The equipment consists of two linear actuators (NLS4, Newmark Systems) that can apply tensile or compressive displacements, a force sensor (LSB200, FUTEK), a high-resolution source-meter, and an LCR meter. Tensile stress-strain measurements were typically conducted at 0.33 mm/s. All rheological measurements were obtained by a rotational rheometer (DHR-3, TA Instruments) with a 25 mm parallel plate geometry. The temperature is maintained at 23 °C using a Peltier plate. To measure the complex moduli ( $G'$  and  $G''$ ), oscillation stress sweep measurement was conducted over a shear stress ranging from  $10^{-2}$  to  $10^4$  Pa. And the flow measurement was performed over a shear rates range of  $10^{-4}$ – $10^2$  s $^{-1}$  to explore the viscosity of inks. Frequency variation of output voltage was measured by an oscilloscope (Keysight DSOX1204G).

### Hybrid 3D printing

Printing was achieved through 3D axis control, which consists of a 2D controller (ShopBot CNC) and three independent z-axes, allowing for multi-material printing with three different inks. The inks were

extruded through a pneumatic-driven extrusion and were regulated by digital pneumatic regulators (Ultimus V High Precision Dispenser, EFD; Pressure Controller, Alicat). The substrate inks were dispensed using 410  $\mu$ m tapered dispense tips (EFD), while the artificial mechanoreceptor ink and conductive ink were dispensed using 410  $\mu$ m stainless steel dispensing tips (EFD). The automated pick-and-place function was performed using an empty syringe with 840  $\mu$ m tapered dispense tips (EFD). A Pneumatic Negative Pressure Generator was used to create a negative pressure that picks up electrical components, and then the generator was turned off to place the electrical component at the desired location.

The pneumatic actuator was fabricated using stiff substrate ink, soft substrate ink, and a PEG-based sacrificial ink. A hot plate integrated into the printing platform was maintained at 120 °C to provide a thermally controlled environment during printing. The actuator base was first printed using the stiff substrate ink via 410  $\mu$ m tapered dispense tips. Soft substrate ink was then printed around a predefined cavity area. This cavity was subsequently filled with PEG-based ink using 410  $\mu$ m stainless steel dispensing tips, followed by a final soft substrate ink layer to fully encapsulate the structure. After curing, the PEG-based ink was manually removed by flushing out with ethanol using a needle. Lastly, a pneumatic tube was inserted to connect the actuator to an external pressure source.

### Data availability

All data supporting the findings of this study are available within the article and its Supplementary Information files. Experimental data generated in this study have been deposited in the Figshare repository (<https://doi.org/10.6084/m9.figshare.29636684>).

### References

1. Kwon, S. M. et al. Environment-adaptable artificial visual perception behaviors using a light-adjustable optoelectronic neuromorphic device array. *Adv. Mater.* **31**, 1906433 (2019).
2. Sun, F., Lu, Q., Feng, S. & Zhang, T. Flexible artificial sensory systems based on neuromorphic devices. *ACS Nano* **15**, 3875–3899 (2021).
3. Safa, A., Van Assche, J., Alea, M. D., Catthoor, F. & Gielen, G. G. E. Neuromorphic near-sensor computing: from event-based sensing to edge learning. *IEEE Micro* **42**, 88–95 (2022).
4. Lele, A., Fang, Y., Ting, J. & Raychowdhury, A. An end-to-end spiking neural network platform for edge robotics: from event-cameras to central pattern generation. *IEEE Trans. Cogn. Dev. Syst.* **14**, 1092–1103 (2022).
5. Zhang, G. et al. Spiking neural networks in intelligent edge computing. *IEEE Consum. Electron. Mag.* **2162**, 2248 (2024).
6. Yang, J.-Q. et al. Neuromorphic engineering: from biological to spike-based hardware nervous systems. *Adv. Mater.* **32**, 2003610 (2020).
7. Park, H. L. et al. Flexible neuromorphic electronics for computing, soft robotics, and neuroprosthetics. *Adv. Mater.* **32**, 1903558 (2020).
8. Tee, B. C. K. et al. A skin-inspired organic digital mechanoreceptor. *Science* **350**, 313–316 (2015).
9. Liu, X. et al. Neuromorphic nanoionics for human–machine interaction: from materials to applications. *Adv. Mater.* **36**, 2311472 (2024).
10. Shim, H. et al. Stretchable elastic synaptic transistors for neurologically integrated soft engineering systems. *Sci. Adv.* **5**, 4961–4972 (2019).
11. Lee, Y. et al. A low-power stretchable neuromorphic nerve with proprioceptive feedback. *Nat. Biomed. Eng.* **7**, 511–519 (2022).
12. Huynh, H. Q. et al. Bio-inspired artificial fast-adaptive and slow-adaptive mechanoreceptors with synapse-like functions. *Adv. Funct. Mater.* **33**, 2303535 (2023).

13. Kim, Y. et al. A bioinspired flexible organic artificial afferent nerve. *Science* **360**, 998–1003 (2018).
14. Seo, S. et al. Artificial optic-neural synapse for colored and color-mixed pattern recognition. *Nat. Commun.* **9**, 5106 (2018).
15. Ni, Y. et al. An artificial nerve capable of UV-perception, NIR-vis switchable plasticity modulation, and motion state monitoring. *Adv. Sci.* **9**, 2102036 (2022).
16. Yuan, R. et al. A neuromorphic physiological signal processing system based on VO<sub>2</sub> memristor for next-generation human-machine interface. *Nat. Commun.* **14**, 3695 (2023).
17. Berthoud, H. R. Anatomy and function of sensory hepatic nerves. *Anat. Rec. A* **280**, 827–835 (2004).
18. Wang, K., Jia, Y. & Yan, X. A biomimetic afferent nervous system based on the flexible artificial synapse. *Nano Energy* **100**, 107486 (2022).
19. Someya, T. & Amagai, M. Toward a new generation of smart skins. *Nat. Biotechnol.* **37**, 382–388 (2019).
20. Wang, M. et al. Artificial skin perception. *Adv. Mater.* **33**, 2003014 (2021).
21. He, K., Wang, C., He, Y., Su, J. & Chen, X. Artificial neuron devices. *Chem. Rev.* **123**, 13796–13865 (2023).
22. Wang, W. et al. Neuromorphic sensorimotor loop embodied by monolithically integrated, low-voltage, soft e-skin. *Science* **380**, 735–742 (2023).
23. Chun, S. et al. An artificial neural tactile sensing system. *Nat. Electron.* **4**, 429–438 (2021).
24. Jiang, C. et al. A flexible artificial sensory nerve enabled by nanoparticle-assembled synaptic devices for neuromorphic tactile recognition. *Adv. Sci.* **9**, 2106124 (2022).
25. Zhang, C. et al. Bioinspired artificial sensory nerve based on Nafion memristor. *Adv. Funct. Mater.* **29**, 1808783 (2019).
26. Yu, F. et al. Artificial tactile perceptual neuron with nociceptive and pressure decoding abilities. *ACS Appl. Mater. Interfaces* **12**, 26258–26266 (2020).
27. Kang, K. et al. Bionic artificial skin with a fully implantable wireless tactile sensory system for wound healing and restoring skin tactile function. *Nat. Commun.* **15**, 10 (2024).
28. Fu, S. et al. Fabrication of large-area bimodal sensors by all-inkjet-printing. *Adv. Mater. Technol.* **4**, 1800703 (2019).
29. Tan, H. et al. Tactile sensory coding and learning with bio-inspired optoelectronic spiking afferent nerves. *Nat. Commun.* **11**, 1369 (2020).
30. Ntagios, M., Nassar, H., Pullanchiyodan, A., Navaraj, W. T. & Dahiya, R. Robotic hands with intrinsic tactile sensing via 3D printed soft pressure sensors. *Adv. Intell. Syst.* **2**, 1900080 (2020).
31. Valentine, A. D. et al. Hybrid 3D printing of soft electronics. *Adv. Mater.* **29**, 1703817 (2017).
32. Khan, Y. et al. A new frontier of printed electronics: flexible hybrid electronics. *Adv. Mater.* **32**, 1905279 (2020).
33. Woodman, S. J., Shah, D. S., Landesberg, M., Agrawala, A. & Kramer-Bottiglio, R. Stretchable arduinos embedded in soft robots. *Sci. Robot* **9**, eadn6844 (2024).
34. Ding, S. et al. Pressure-sensitive behaviors, mechanisms and model of field assisted quantum tunneling composites. *Polymer* **113**, 105–118 (2017).
35. Dhote, S., Behdian, K., Andrysek, J. & Bian, J. Experimental investigation of a hybrid nickel-carbon black polydimethylsiloxane conductive nanocomposite. *J. Compos. Mater.* **54**, 2051–2063 (2020).
36. Shi, L. et al. Quantum effect-based flexible and transparent pressure sensors with ultrahigh sensitivity and sensing density. *Nat. Commun.* **11**, 3529 (2020).
37. Yun, G. et al. Liquid metal composites with anisotropic and unconventional piezoconductivity. *Matter* **3**, 824–841 (2020).
38. Lee, K.-C. et al. Artificial mechanoreceptor based on van der Waals stacking structure. *Matter* **4**, 1598–1610 (2021).
39. Rydqvist, B. & Swerup, C. Stimulus-response properties of the slowly adapting stretch receptor neuron of the crayfish. *Acta Physiol. Scand.* **143**, 11–19 (1991).
40. Duduta, M. et al. Multilayer dielectric elastomers for fast, programmable actuation without prestretch. *Adv. Mater.* **28**, 8058–8063 (2016).
41. Lantada, A. D., Lafont, P., Sanz, J. L. M., Munoz-Guijosa, J. M. & Otero, J. E. Quantum tunnelling composites: Characterisation and modelling to promote their applications as sensors. *Sens. Actuators A Phys.* **164**, 46–57 (2010).
42. Stassi, S. & Canavese, G. Spiky nanostructured metal particles as filler of polymeric composites showing tunable electrical conductivity. *J. Polym. Sci. Part B Polym. Phys.* **50**, 984–992 (2012).
43. Bloor, D., Donnelly, K., Hands, P. J., Laughlin, P. & Lussey, D. A metal-polymer composite with unusual properties. *J. Phys. D. Appl. Phys.* **38**, 2851 (2005).
44. Kchit, N. & Bossis, G. Electrical resistivity mechanism in magnetorheological elastomer. *J. Phys. D. Appl. Phys.* **42**, 105505 (2009).
45. Yun, G. et al. Electro-mechano responsive elastomers with self-tunable conductivity and stiffness. *Sci. Adv.* **9**, eadf1141 (2023).
46. Duan, L., D'hooge, D. R. & Cardon, L. Recent progress on flexible and stretchable piezoresistive strain sensors: From design to application. *Prog. Mater. Sci.* **114**, 100617 (2020).
47. Tian, T. & Nakano, M. Fabrication and characterisation of anisotropic magnetorheological elastomer with 45° iron particle alignment at various silicone oil concentrations. *J. Intell. Mater. Syst. Struct.* **29**, 151–159 (2018).
48. Khairi, M. H. A. et al. Enhancement of particle alignment using silicone oil plasticizer and its effects on the field-dependent properties of magnetorheological elastomers. *Int. J. Mol.* **20**, 4085 (2019).
49. Wei, D., Liao, B., Huang, J., Zhang, M. & Pang, H. Fabrication of castor oil-based hyperbranched urethane acrylate UV-curable coatings via thiol-ene click reactions. *Prog. Org. Coat.* **135**, 114–122 (2019).
50. Niu, X. et al. Synthesizing a new dielectric elastomer exhibiting large actuation strain and suppressed electromechanical instability without prestretching. *J. Polym. Sci. B Polym. Phys.* **51**, 197–206 (2013).
51. Li, Q., Zhou, H. & Hoyle, C. E. The effect of thiol and ene structures on thiol-ene networks: Photopolymerization, physical, mechanical and optical properties. *Polymer* **50**, 2237–2245 (2009).
52. Saadi, M. A. S. R. et al. Direct ink writing: a 3D printing technology for diverse materials. *Adv. Mater.* **34**, 2108855 (2022).
53. Gray, J. A. B. & Sato, M. Properties of the receptor potential in Pacinian corpuscles. *J. Physiol.* **122**, 610 (1953).
54. Koga, K. et al. Selective activation of primary afferent fibers evaluated by sine-wave electrical stimulation. *Mol. Pain.* **1**, 1744–8069 (2005).
55. Améduri, B., Boutevin, B. & Kostov, G. Fluoroelastomers: synthesis, properties and applications. *Prog. Polym. Sci.* **26**, 105–187 (2001).
56. Xue, Z. et al. Mechanically-guided structural designs in stretchable inorganic electronics. *Adv. Mater.* **32**, 1902254 (2020).
57. Yang, J. C. et al. Geometrically engineered rigid island array for stretchable electronics capable of withstanding various deformation modes. *Sci. Adv.* **8**, 3863 (2022).
58. Hou, S. et al. Stretchable electronics with strain-resistive performance. *Small* **20**, 2306749 (2024).
59. Choi, S., Han, S. I., Kim, D., Hyeon, T. & Kim, D. H. High-performance stretchable conductive nanocomposites: materials, processes, and device applications. *Chem. Soc. Rev.* **48**, 1566–1595 (2019).
60. Yang, C. et al. Silver surface iodination for enhancing the conductivity of conductive composites. *Adv. Funct. Mater.* **20**, 2580–2587 (2010).

61. Chortos, A., Hajiesmaili, E., Morales, J., Clarke, D. R. & Lewis, J. A. 3D printing of interdigitated dielectric elastomer actuators. *Adv. Funct. Mater.* **30**, 1907375 (2020).
62. Guo, S. Z., Qiu, K., Meng, F., Park, S. H. & McAlpine, M. C. 3D printed stretchable tactile sensors. *Adv. Mater.* **29**, 1701218 (2017).
63. Lebel, L. L., Aissa, B., El Khakani, M. A. & Therriault, D. Ultraviolet-assisted direct-write fabrication of carbon nanotube/polymer nanocomposite microcoils. *Adv. Mater.* **22**, 592–596 (2010).
64. Larson, N. M. et al. Rotational multimaterial printing of filaments with subvoxel control. *Nature* **613**, 682–688 (2023).
65. Rios, O. et al. 3D printing via ambient reactive extrusion. *Mater. Today Commun.* **15**, 333–336 (2018).

## Acknowledgements

This work was supported by the startup package at Purdue University from A.C. and NSF grant 2301509 and was partially supported by the National Science Foundation through Harvard University's Materials Research Science and Engineering Center DMR-2011754. M.L. acknowledges the support of the Asan Fellowship.

## Author contributions

Conceptualization: M.L., M.S. and A.C.; Methodology: M.L., M.S. and A.C.; Investigation: M.L., M.S., J.W. and A.C.; Visualization: M.L.; Funding acquisition: A.C.; Project administration: A.C.; Supervision: A.C.; Writing-original draft: M.L.; Writing-review and editing: M.L., M.S., J.W. and A.C.

## Competing interests

The authors declare no competing interests.

## Additional information

**Supplementary information** The online version contains supplementary material available at <https://doi.org/10.1038/s41467-025-63470-7>.

**Correspondence** and requests for materials should be addressed to Alex Chortos.

**Peer review information** *Nature Communications* thanks Kyowon Kang and the other, anonymous, reviewers for their contribution to the peer review of this work. A peer review file is available.

**Reprints and permissions information** is available at <http://www.nature.com/reprints>

**Publisher's note** Springer Nature remains neutral with regard to jurisdictional claims in published maps and institutional affiliations.

**Open Access** This article is licensed under a Creative Commons Attribution-NonCommercial-NoDerivatives 4.0 International License, which permits any non-commercial use, sharing, distribution and reproduction in any medium or format, as long as you give appropriate credit to the original author(s) and the source, provide a link to the Creative Commons licence, and indicate if you modified the licensed material. You do not have permission under this licence to share adapted material derived from this article or parts of it. The images or other third party material in this article are included in the article's Creative Commons licence, unless indicated otherwise in a credit line to the material. If material is not included in the article's Creative Commons licence and your intended use is not permitted by statutory regulation or exceeds the permitted use, you will need to obtain permission directly from the copyright holder. To view a copy of this licence, visit <http://creativecommons.org/licenses/by-nc-nd/4.0/>.

© The Author(s) 2025